

Совместное использование метеорологических (WSR-88D) радаров, геостационарных (GOES-R) спутников и измерителей молний для исследования микрофизических характеристик ураганов

Д. Ху⁽¹⁾, А. Рыжков⁽¹⁾, Д. Розенфельд⁽²⁾, П. Жанг⁽¹⁾

⁽¹⁾Университет Оклахомы, США;

⁽²⁾Еврейский университет Иерусалима, Израиль

Основной ущерб от ураганов на суше возникает вследствие наводнений, которые недостаточно прогнозируются в рамках динамических моделей. В данном докладе анализируется микрофизика осадков, вызванных ураганом Харви (2017) в центре («глазе») урагана и в удаленных от центра полосах дождя. В работе используется новая схема представления многоканальной информации спутника GOES-16, вертикальные профили поляризационных радарных параметров (CVP) и данные о молниях получаемых со спутников и наземных сетей. По спутниковым данным, удаленные от центра полосы осадков характеризуются более мощной конвекцией по сравнению с центром урагана, в котором восходящие потоки слабее в силу более интенсивного сдвига ветра. Вертикальные профили радарных поляризационных параметров также подтверждают, что восходящие движения в удаленных полосах осадков сильнее и размеры ледяных частиц вблизи их вершин больше. Таким образом, осадки, связанные с «глазом» урагана, формируются в непосредственной близости от поверхности (классический теплый тропический дождь). В то же время существенная часть осадков вдали от центра урагана формируется также за счет таяния большого количества льда, что увеличивает интенсивность дождя и повышает вероятность наводнения.

Synergetic use of the WSR-88D radars, GOES-R satellites, and lightning networks to study microphysical characteristics of hurricanes.

Jiaxi Hu⁽¹⁾, Alexander Ryzhkov⁽¹⁾, Daniel Rosenfeld⁽²⁾, and Pengfei Zhang⁽¹⁾

⁽¹⁾University of Oklahoma, USA;

⁽²⁾The Hebrew University of Jerusalem, Israel

Much of the damage from landfalling hurricanes is inflicted by the excessive flooding, which is not fully understood based on dynamic considerations alone. This study analyzes the microphysics and precipitation patterns of hurricane Harvey (2017) in both eyewall and outer rain band regions. The techniques include newly developed Geostationary Operational Environmental Satellite 16 (GOES-R) multi-channel convective Red Green Blue (RGB) scheme, WSR-88D dual-polarization Column-Vertical Profiles (CVP) products, lightning data from both ground-based Lightning Mapping Array (LMA) and the Geostationary Lightning Mapper (GLM) onboard of GOES-R. Based on the satellite RGB scheme, the outer rain bands show strong convective structure and the inner eyewall has less convective vigor, which is likely due to the strong vertical wind shear that prohibits fast vertical motions. The WSR-88D CVPs further confirm that the outer rain band clouds have strong vertical motion and large ice phase hydrometeors formation aloft, which correlates well with 3D LMA source counts in height and time. The inner eyewall region is dominated by warm rain, whereas the external rain band region has more intense mixed-phase precipitation, which potentially can result in flash flood.

Introduction

From 1851 to 2017, 292 hurricanes directly hit mainland U.S. coastline and 91 of them are categorized as major hurricanes (NOAA 2018). Landfalling hurricanes bring high winds, storm surge, flooding and tornadoes, which make them the costliest natural disasters on Earth for human life and properties. The severity of hurricanes often refers to their maximum wind speed [1]. Yet, the major casualty and property loss are mainly caused by the heavy precipitation and flooding that come with the hurricanes, which are weakly related to the wind speeds.

Hurricane Harvey started as a weak tropical storm and intensified into a category 4 hurricane before landing near Corpus Christi, Texas on August 25, 2017. Harvey stalled at southeast Texas for 5 days and produced more than 60 inches (1.52 m) of precipitation within the Houston metropolitan area. At least 68 direct fatalities are confirmed and 36 of them were in the Houston urban area due to floods. The total estimated cost by Harvey is \$125 billion dollars and ranking number two among most expensive hurricanes in the U.S. history [2].

Previous observational studies of the precipitation and microphysical structures of tropical cyclones (TCs) included mainly single-polarization radar [3, 4] and dual-polarization radars [5, 6, 7]. Compared with the traditional single-polarization radars, the new dual-polarization radars can provide rich information about hydrometeor number concentrations, size, shape, orientation, and dielectric properties within each radar volume scan. These features can be used to distinguish between liquid and ice phase hydrometeors under different microphysical and dynamical processes [8, 9].

Satellite remote sensing techniques have also been applied for understanding the mechanisms that control TCs genesis and intensification [10, 11]. The newly launched Geostationary Operational Environmental Satellite R Series (GOES-R) satellite provides data at 16 different Advanced Baseline Imager channels with spatial resolutions from 500 meters to 2 km and temporal resolutions from 30 seconds to 15 minutes over much of the continental US. Geostationary Lightning Mapper (GLM) is the first operational lightning mapper ever in geostationary orbit on board of GOES-R satellite. The flash data can be used as a good indicator of convection intensity. Previous remote sensing efforts [12, 13, 14, 15, 16] have shown great potential for the study of TCs microphysical structure by using polar orbit satellite. These methods can be applied to GOES-R for providing microphysical understanding in combination with the state-of-the-art geostationary time evolution of hurricane systems similar to operational WSR-88D radar network.

Surface precipitation is strongly influenced by the upper storm microphysical processes [17]. This study will focus on using a combination of satellite and radar observations in understanding TCs microphysical structure and precipitation patterns. Methodology

1.1.1. GOES-R data and processing

1.1.1.1. Convective RGB Scheme

Inherited from the previous Rosenfeld - Lensky Technique (RLT) [15], the new GOES-R version of convective RGB displays reflectance [%] in the solar channels and brightness temperature (BT) [K] in the thermal channels.

The RGB channels information is given in Table 1. The 0.86 μm reflectance (r0.86) in red approximates the cloud optical depth and the amount of vertically integrated cloud water and ice [13], since 0.86 μm channel is much less absorbed by cloud droplets compared with IR bands. The 1.6 μm reflectance (r1.6) in green estimates the cloud top ice crystals size and concentration. The 10.4 μm BT (T10.4) modulates the blue that refers to the cloud top temperature. All RGB channels percentiles are from 0.1 to 99.9 in order to exclude outliers. For the green channel, the color

percentile calculation is based on pixels with 10.4 μm BT less than 233.15 K (homogenous freezing temperature) in order to focusing on icy cloud tops.

Table 1. Convective RGB Scheme layout (Lensky and Rosenfeld 2008). The scheme channels information, stretch values and percentile ranges are provided.

| | GOES-R Quantity | Stretch | Percentile |
|-------|--------------------|----------------|--|
| Red | r0.86 | $\Gamma = 0.5$ | 0.1-99.9 |
| Green | r1.6 | $\Gamma = 0.5$ | 0.1-99.9 (10.4 μm BT < 233.15K) |
| Blue | T10.4 | $\Gamma = 1.5$ | 0.1-99.9 |

Different Γ values are applied to stretch the three beams base on physical considerations. $\Gamma < 1$ stretches the colors of the larger values on expense of the low values, while $\Gamma > 1$ does the opposite. For red and green, $\Gamma = 0.5$ enhances the cloud pixels with deeper cloud optical depth (r0.86) and cloud top with higher concentration of small ice crystals (r1.6). For the blue beam, $\Gamma = 1.5$ delineates the colder and taller cloud top pixels (T10.4).

This color scheme is useful for convective cloud identification. In this color scheme ocean appears blue (point A in Fig. 1a) because sea surface is warm with high T10.4 only. Cirrocumulus (point B in Fig. 1a) appear greenish because they are optically thin (low r0.86), with high cloud top (relatively low T10.4) and small ice crystals (high r1.6). Convective cores (point C in Fig. 1a) has extremely cold cloud top (low T10.4), high cloud optical depth (high r0.86) and large number of small ice crystals (high r1.6), which make them yellow. Point E (Fig. 1a) shows the non-convective clouds (purple) with warm cloud top (high T10.4), large amount of vertically integrated cloud water (high r0.86) and almost no ice at cloud top (low r1.6). The non-convective cores (point D in Fig. 1a, Harvey eyewall) has similar features similar to the external convective band (point C in Fig. 1a) in all three bands and the differences lies in the convective state or the roughness of cloud top, as apparent by the spatial variability of the texture, or boiling appearance. The roughness of each 2D GOES-R snapshot pixel is quantified by the surrounding 3-by-3 r1.6 samples' standard deviation [18]. The cloud edge pixels are ignored for the roughness calculation. Comparison of C and D regions shows obvious difference of cloud top roughness (Fig. 1b). Clouds with deep vertical development share the same features of large water content, cold cloud top and high concentration of small ice crystals, but the enhanced roughness at the cloud top indicates stronger vertical motions.

1.1.1.2. Geostationary Lightning Mapper (GLM) Data

The GLM on board of the GOES-R satellite uses a single-channel (777.4 nm) near-infrared optical transient detector for optical scene change detection every 2 ms. The GLM data spatial resolution is about 10 km with 90% flash detection efficiency and a 20-second product latency.

In this study, the 15-minutes full-disk GOES-R data are used as snapshots of hurricane Harvey's cloud top convective features. The GLM +/- 7.5 minutes of data were overlaid on each RGB image. The GLM parameters such as flash energy and flash location are used in this study.

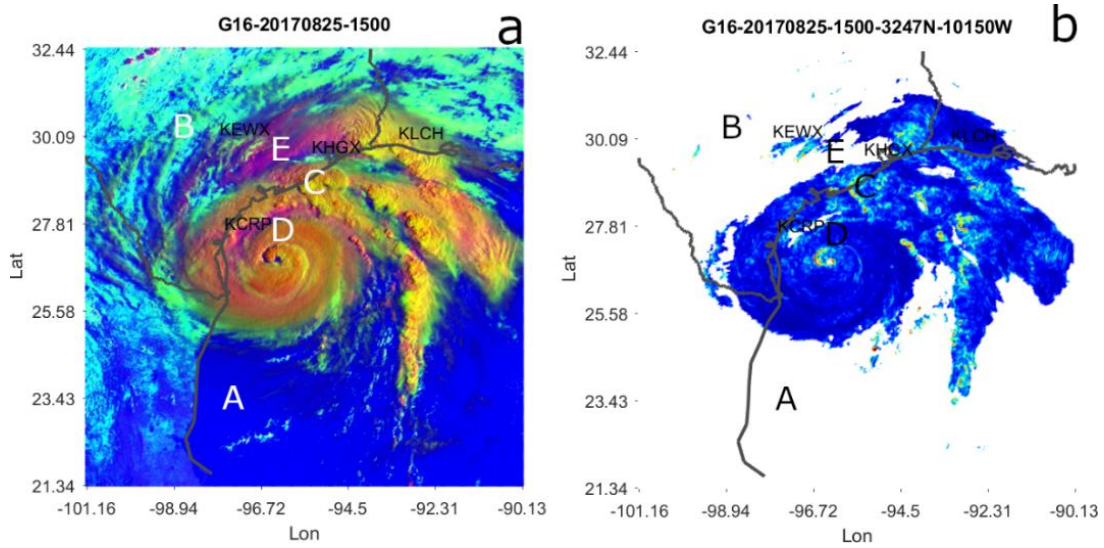


Fig.1. GOES-R convective RGB scheme example (a) and corresponding roughness map (b) of hurricane Harvey at 1500 UTC, August 25, 2017.

1.1.2. Next-Generation Radar (NEXRAD) data and processing

1.1.2.1. Polarimetric variables and retrieved products

A standard set of radar variables measured by the WSR-88D radars is used in the study. These include radar reflectivity Z , differential reflectivity Z_{DR} , specific differential phase K_{DP} , and cross-correlation coefficient ρ_{hv} .

The mean volume diameter D_m and total number concentration N_t of ice particles have been estimated using polarimetric radar retrieval techniques. D_m and N_t are retrieved from the combination of Z , K_{DP} and Z_{DR} as defined by Bukovcic et al. [19] and Ryzhkov and Zrnicek (2019) [9]. The value of D_m is determined as

$$D_m = -0.1 + 2.0\eta \quad (1)$$

where

$$\eta = \left(\frac{Z_{DP}}{K_{DP}\lambda} \right)^{1/2} \quad (2)$$

In (2), Z_{DP} is the reflectivity difference defined as the difference between radar reflectivity factors Z_h and Z_v at orthogonal polarizations expressed in a linear scale. Hence, the units of Z_{DP} are mm^6m^{-3} . K_{DP} is expressed in deg km^{-1} and the radar wavelength λ is in mm.

The total number concentration of ice particles is determined from equation

$$\log(N_t) = 0.1Z(\text{dBZ}) - 2\log(\gamma) - 1.33. \quad (3)$$

where

$$\gamma = 0.78 \frac{Z_{DP}}{K_{DP}\lambda}. \quad (4)$$

The advantage of using retrieval relations (1) – (4) in ice is that they are practically insensitive to the variability of the particles' shapes and orientations. These have been derived on the assumption that the density of ice / snow is inversely proportional to the volume diameter of ice particle

$$\rho_s = \alpha D^{-1} \quad (5)$$

where the multiplier α is proportional to the degree of riming. This means that the suggested retrieval relations are not valid in graupel / hail.

Because the measured values of K_{DP} and Z_{DR} are quite noisy in ice / snow, some additional spatial averaging of K_{DP} and Z_{DR} is needed to reduce statistical errors of their estimates. Azimuthal averaging of radar variables in a full 360° circle or in a limited azimuthal sector is at the core of recently developed techniques for processing and representing polarimetric radar variables such as quasi-vertical profiles (QVP) [20, 21, 22], range-dependent QVP (or RD-QVP) [23], or EVP [16]. The vertical profiles of major radar variables (Z , Z_{DR} , K_{DP} , and ρ_{hv}) as well as the retrieval products D_m and N_t are commonly represented in a height vs time format which allows to examine temporal evolution of the vertical structure of the storm.

1.1.2.2. Columnar-Vertical Profile (CVP)

QVP, RD-QVP, and EVP are radar-centric products. Murphy et al. offers a novel technique called Columnar-Vertical Profile (CVP) that allows estimating average vertical profiles of radar variables within a vertical column centered at an arbitrary location within the radar coverage area.

The CVP technique prescribes azimuthal averaging in a limited azimuthal sector and radial interval enclosing a center of the CVP column using all available tilts of radar data. The averaged data from each radar tilt at various distances and heights from radar are projected along the horizontal to the center CVP location. The output after this process is a single column of CVP consisting of all data at each elevation angle with varying heights at the same horizontal location in radius and azimuth from the given radar. This averaging and projection process of data is repeated for each radar volume scan elevation angle without any weighting or interpolation. The selected sector in this study spans 20 km in range and 20° in azimuth around the center of the selected CVP column. The locations of the selected CVP sectors are shown in Fig. 2. The CVP time resolution follows the radar volume scan frequency on the order of every 5 minutes. Detailed CVP method description can be found in Murphy.

1.2. Lightning Mapping Array (LMA)

The Houston LMA consists of 12 time-of-arrival lightning sensors operating in the Very High Frequency (VHF) television band (e.g. 60-66 MHz) and using the time of arrival events at each LMA site to produce 3-dimensional lightning discharges data set. The temporal and spatial resolutions of LMA are 80 μ s and 10⁻⁶ degree. The quality control is to exclude data points with chi-square values of their triangulation less than 1.0. The integrated event counts are prepared for each CVP time-height pixels with the same CVP sector area and radar volume scan temporal resolution.

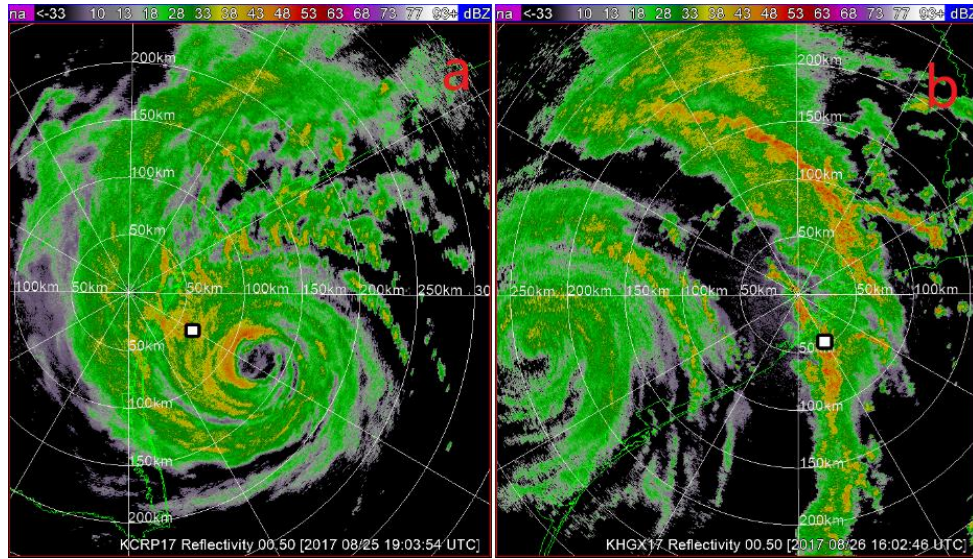


Fig.2. Radar 0.5-degree reflectivity plan position indicator (PPI) maps. (a) Harvey's inner eyewall and (b) Harvey's outer rain band. Radar CVP sectors are labelled by the white boxes in all radar PPI panels.

1.3.High-Resolution Rapid Refresh (HRRR) model Data

The HRRR is a NOAA real-time atmospheric model with 3-km resolution, hourly updated, cloud-resolving, convection-allowing scheme, initialized by 3 km grids with 3 km radar assimilation. Radar data are assimilated in the HRRR every 15 min over a 1-h period adding further detail to that provided by the hourly data assimilation from the 13 km radar-enhanced Rapid Refresh simulations. The hourly updated HRRR data gives the estimate of 0° C, -15° C and -40° C isotherms' heights. The closest HRRR data point to the CVP location center is used to depict the height of the isotherms.

2. Conceptual Model and Hypothesis

An observational dataset is combined synergistically in this study and we took the advantage of the rich information to investigate the cloud and precipitation microphysical structure in the hurricane eyewall region and the external rain bands.

The hurricane eyewall region (Fig. 3a) has strong vertical wind shear that greatly weakens vertical motion and tilts the cloud hydrometeors transport pathway. The aerosol source here is mainly from hurricane force wind driven heavy sea spray, which provides large number of aerosol particles, including ultrafine aerosol particles (UAP), which are too small for nucleating cloud drops at its base. Large number of UAPs are activated further aloft and create large number of small ice crystals at cloud top. The precipitation in this region is dominated by warm rain, which is enhanced by the larger sea spray particles. Melting ice hydrometeors add to the rainfall, but do not dominate it.

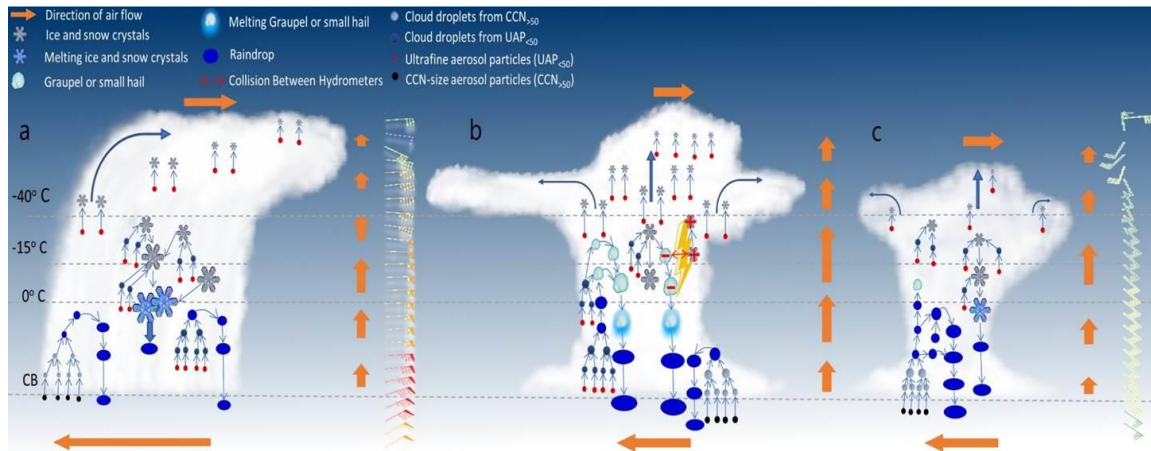


Fig. 3. Conceptual plot illustrating microphysical differences between three different scenarios of rain formation (see explanation in the text)

The external rain bands outside the main circulation of the hurricane occur with much weaker surface wind speeds that raise little sea spray aerosols. Large concentrations of UAPs may still come from sources such as anthropogenic air pollution, including possibly the oil rigs in the Gulf of Mexico. A cartoon illustrating microphysical composition of the hurricane external rain bands with high and low UAP concentration scenario is shown in Fig. 3 (panels 3b and 3c, respectively). In general, the outer rain bands region has an order of magnitude smaller vertical wind shear, which favors convection development and strong vertical motions. For the high UAP scenario (Fig. 3b), according to Fan et al. [24], the activation of UAPs above cloud base in clouds with heavy warm rain can enhance condensational heating that invigorates the convection. Stronger vertical motion also facilitates condensation aloft, along with increased upward transport of liquid water content and hydrometeors, which stimulates mixed phase hydrometeor formation. The latent heat release from liquid to ice further enhances convection [15], which creates overshooting tops and anvil clouds aloft. The enhanced ice phase formation includes not only ice crystals but also hail and graupel. The collision between hail/graupel and ice crystals due to their differences in terminal velocity within a supercooled water environment can lead to charge separation and lightning discharges. Hail/graupel falling below ML melts into raindrops and may contribute significantly to the surface rain rate whereby increasing flash flood potential.

The low UAP scenario (Fig. 3c) of external rain band clouds implies less vertical development due to the lack of condensational heating with decreased UAP concentration. The cloud tops are lower with no obvious overshooting tops and weaker anvil clouds. The precipitation type is determined by both warm rain and mixed phase precipitation processes. The source of raindrops can be either from coalescence of cloud droplets or melted ice particles aloft. Since the vertical motion is weaker in the low UAP scenario, hail/graupel seldom forms due to the lack of water content and ice crystals. Less lightning activity is expected in the low UAP scenario.

3. Results

3.1. GOES-R observations of Harvey

The convective RGB scheme was applied to hurricane Harvey, as shown in Fig. 4. Figure 4a is a snapshot of Harvey over an open ocean at 15:00 UTC on August 24, 2017 with the GLM data overlaid at the same time in Fig. 4b. The eye was not obvious at this time (Figs. 4a, b) because Harvey was quickly intensifying and large mass of deep convection formed over the center [25].

This can be inferred from the yellow rough cloud top signatures by the east eyewall region. The added GLM flash dots over this region further confirm its strong convective nature.

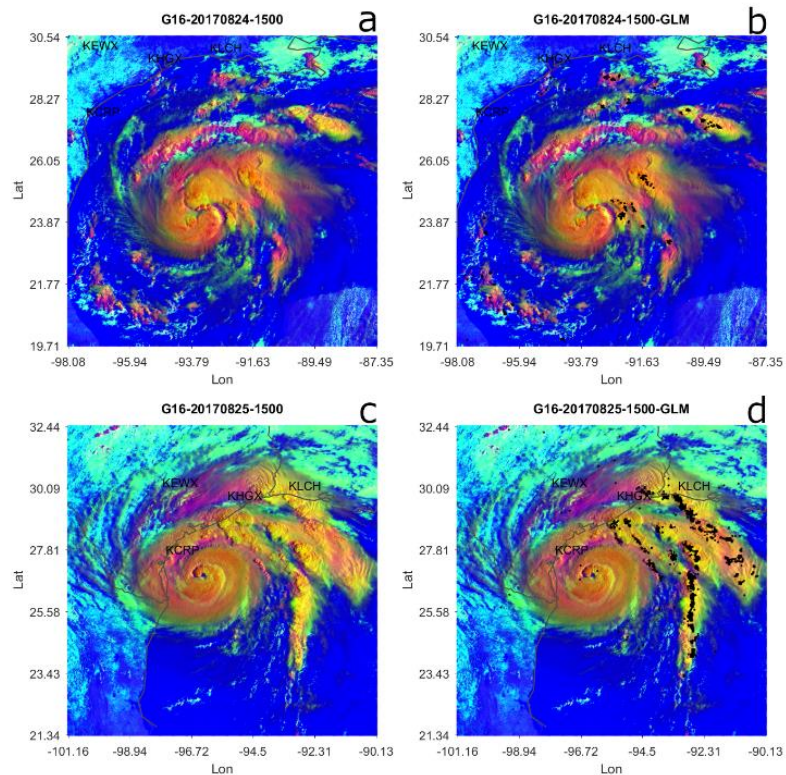


Fig. 4. GOES-R convective RGB snapshots of hurricane Harvey (a,b,c and d). The left column (a and c) shows RGB snapshots only and the right column (b and d) shows RGB snapshots with GLM data. Each black dot represents one GLM flash data point.

By the late 24th August, Harvey intensified into category 3 hurricane with a clear eye (not shown here). On the next day, Harvey further intensified into category 4 and reached southeast Texas coastline (Figs. 4c, d). From the snapshot at 1500 UTC on August 25, 2017, a clear eye and eyewall region with smooth cloud tops is formed. This appearance implies no penetrating strong updrafts overshooting from the cloud tops. The external rain bands in Fig. 4c are marked by high roughness signatures and are highly convective. Figure 4d with GLM flash data overlaid shows clear distinction between convective external rain bands and weaker convective inner core region. The updrafts in the eyewall were probably suppressed by the strong vertical wind shear, which that prevents very strong vertical motions. The clouds that converge to the center of Harvey become less and less convective due to this reason. The external rain bands, which reside outside of the main hurricane circulation intensify as normal squall lines and maintain their highly convective nature.

The separation of intense convective and less-convective regions of a hurricane determines precipitation rate of each region. Harvey stalled after landing for 5 days in southeast Texas. Houston was affected mostly by Harvey's external convective rain bands the entire time after its landfall and received maximum cumulative precipitation in Texas throughout this catastrophic event. It is now clear that in order to better predict and issue warning about hurricanes, focusing only on the track of hurricane eye or core region is not sufficient. The satellite can provide good

indications of the region of intense convection versus the weaker convection, but does not see through the cloud top. It is essential to complement the satellite signatures with radar observations from the ground in order to see the detailed microphysical structure differences between eyewall region and external rain bands within the clouds' vertical columns.

3.2. WSR-88D CVP observations in Harvey

Figure 5 shows the CVPs of Z , Z_{DR} , K_{DP} , ρ_{hv} and retrieved parameters of size distributions D_m and N_t observed close to the eye of Harvey from 1500 UTC to 2211 UTC August 25, 2017. A ρ_{hv} depression at the height around 5 km defines the melting layer (ML) signature in polarimetric CVPs (Fig. 5d). The maximum reflectivity feature from 1829 UTC to 2000 UTC below the ML shows increasing intensity towards the surface. The combination with downward increasing K_{DP} (Fig. 5c) indicates that the surface precipitation is dominated by warm rain process. The overall reflectivity (Fig. 5a) is lower than 20 dBZ above the ML and the ρ_{hv} ML signature is uninterrupted, which indicates weak vertical motions and the non-convective nature in this CVP sector. Note that the D_m and N_t retrieval algorithms work for pure ice phase only and the D_m and N_t estimates are not made within the ML. Above the -15° C isotherm, ice crystals are small (0.1 – 0.5 mm) and their concentration is high (up to 10^3 L $^{-1}$). Based on all previous observations, this distinct warm rain mechanism within the eyewall region usually produces moderate to heavy precipitation, but not as extremely heavy as in the external rain bands, which are discussed next.

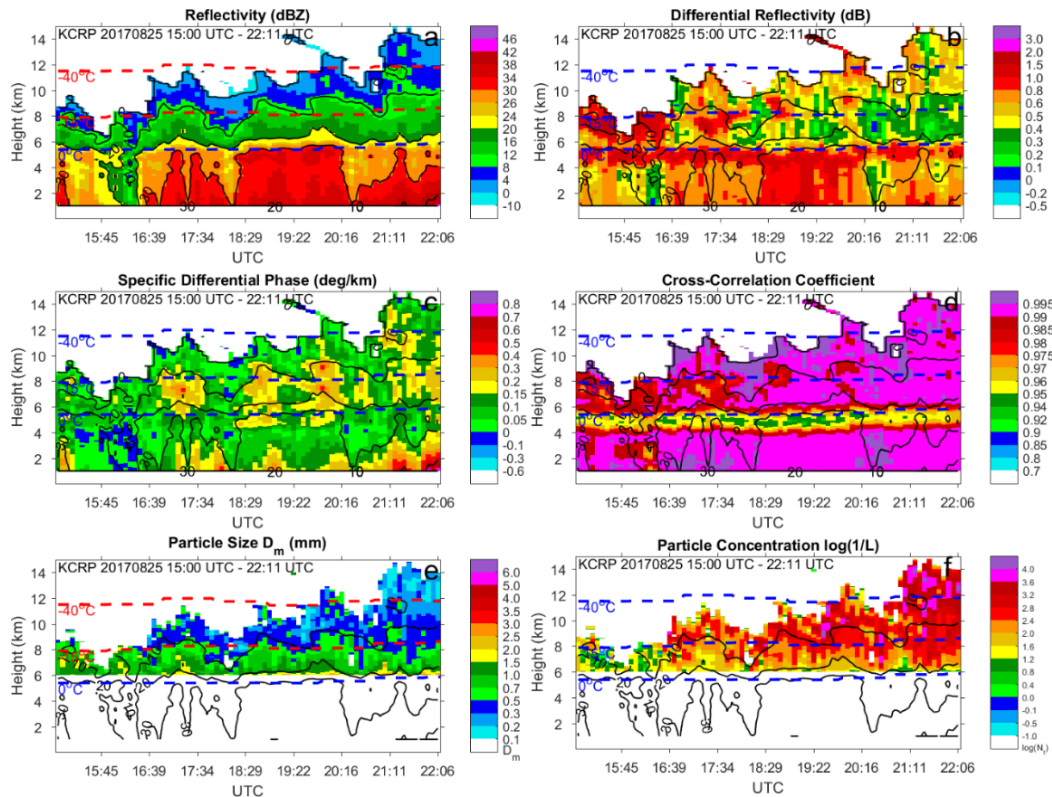


Fig. 5. CVP of Z (a), Z_{DR} (b), K_{DP} (c), ρ_{hv} (d), D_m (e) and N_t (f) of hurricane Harvey eyewall region from 20170825 15:00 UTC to 22:11 UTC. The CVP is centered at 60 km and 120° from the KCRP WSR-88D radar and the CVP base is 20 km in range and 20° in azimuth. The black contours denote reflectivity magnitudes every 10 dBZ. The dot lines in each panel show the corresponding 0° C, -15° C and -40° C isotherms from HRRR.

The CVPs of the external rain band are shown in Fig. 6. The ML identified by ρ_{hv} (Fig. 6d) is also around 5 km height. A black box in each panel encloses the maximum K_{DP} (Fig. 6c) region, which represents maximum precipitation. The downward positive gradient of K_{DP} below ML from 15:43 UTC to 16:30 UTC indicates further enhancement of the precipitation by coalescence of cloud droplets. High values of Z (Fig. 6a) and Z_{DR} (Fig. 6b) black boxes indicate heavy precipitation. The magnitude of ρ_{hv} in the ML is higher in the convective region and represents a common indication of melting graupel or heavily rimed snow (Fig. 6d). As opposed to the eyewall region, Z above the ML exceeds 20 dBZ (Fig. 6a). The combination of these features shows the convective nature in this CVP sector that produces heavy precipitation (38 mm/h from radar QPEs) and the potential for flooding. Besides a coalescence process, size sorting by relatively strong vertical motion documented by Wu et al. [26] can also result in positive downward gradient of Z_{DR} . In the D_m (Fig. 6e) panel over ML, the ice phase hydrometer sizes are much larger than in the eyewall CVP sector (Fig. 5e). Because of relatively large Z (>20 dBZ, Fig. 6a) and almost zero K_{DP} (Fig. 6c) between red and black boxes, the ice phase hydrometers here are likely composed of highly aggregated snow and graupel. The red numbers at the bottom are the $\log_2(\#)$ scaled GLM flash number count in this CVP sector. The occurrence of lightning is consistent with the development of convection here. Interestingly, no GLM lightning flashes were detected in the Harvey's eyewall within the selected CVP sector.

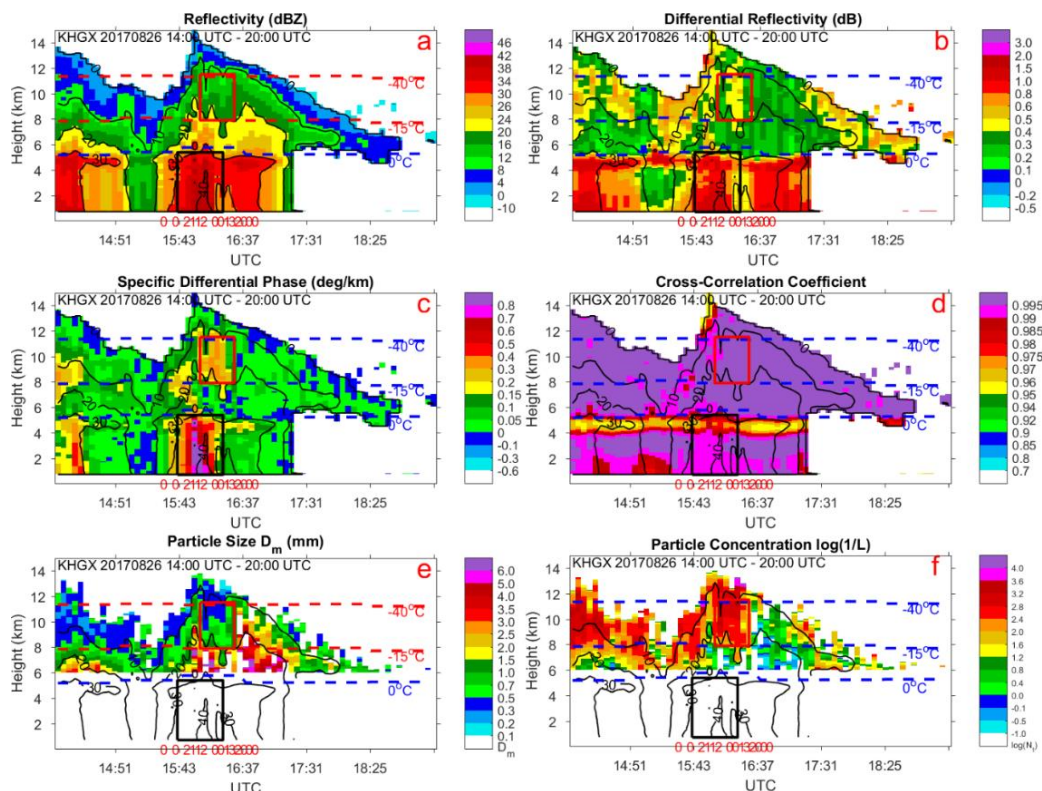


Fig. 6. Same as in Fig. 5, but for hurricane Harvey's external rain bands from 20170826 14:00 UTC to 20:00 UTC. The CVP is centered at 40 km and 150° from the KHXG radar. The red numbers at the bottom of each panel indicate the $\log_2(\#)$ GLM flash count within the CVP sector in each radar volume scan.

In Fig.7, the Houston LMA data are reconstructed to the identical time-height grids as in the CVP columns shown in Fig. 6. The red box is selected around the core of maximum LMA source count. The core of LMA (up to 10^{11} events per CVP pixel) is between -15°C and -40°C isotherms. The red box in Fig. 6 is at the same location as in Fig. 7. Low Z (Fig. 6a, $<20\text{ dBZ}$), high Z_{DR} (Fig. 6b, $>0.4\text{ dB}$) and high K_{DP} (Fig. 6c, $>0.3\text{ deg/km}$) within the red boxes indicate large amount of small ice crystals. The low D_{m} (Fig. 6e, $0.3 - 1\text{ mm}$) and high N_{t} (Fig. 6f, over 10^3 L^{-1}) signature within the red boxes further prove the existence of high concentration of small ice crystals. The traditional charge separation mechanism implied the pre-requisite environment must include ice crystal, graupel and supercooled water. While the radar retrieval of supercooled water is not possible, the co-existence of ice crystals, graupel, and the core of lightning flashes is indicative of supercooled water. The peak of lightning is slightly lagged in time (~ 20 minutes) after the maximum updraft at the lower levels (black box), which is probably the time needed for convection development and ice phase hydrometeor formation at higher altitude.

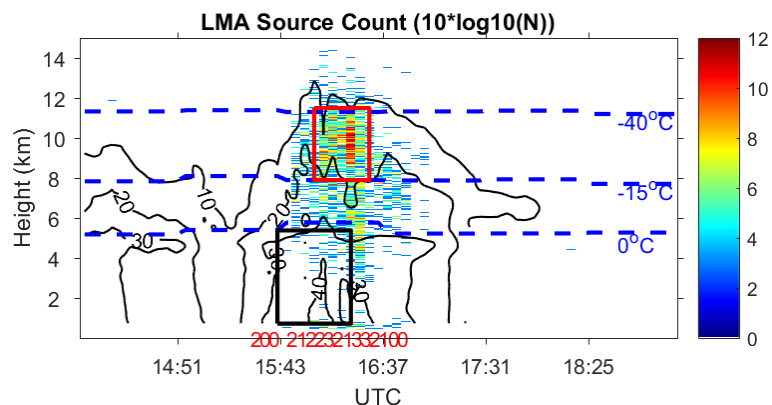


Fig. 7. LMA source count within the same CVP area as in Fig. 6 with identical temporal and spatial resolution. The unit of LMA source count is in dB. Overlaid are the isotherms and reflectivity contours.

4. Conclusions

In this study, we propose a conceptual model emphasizing very different cloud microphysical structures of the eyewall and the external rain bands of hurricanes. The microstructure differences are likely caused by the differences in the strength of the vertical wind shear between the eyewall and the external rain bands.

The newly launched GOES-R satellite provides new insights to the identification of convective vigor by the structure of cloud tops. The relatively smooth tops of the eyewall clouds indicate weaker convection, mostly organized by the hurricane scale winds. The “boiling” appearance of the cloud tops of the external rain bands reveals its highly convective vigor.

The radar CVPs provide detailed time-height observational support for the proposed conceptual model. This is obtained from the ability of dual-polarization radars to retrieve the hydrometeors phase, concentration and sizes. The eyewall precipitation is dominated by tropical warm rain that is formed mostly below the ML. The ice phase hydrometeors in the eyewall region are dominated by high concentration of small ice crystals.

Summarizing, we combined ground-based radar measurements with satellite observations to study hurricane microphysical structure from surface to cloud top. This fills in the gap between these observational techniques and shows good agreement and new insights in understanding the

greatly different cloud microphysical and dynamical structures in hurricane eyewall and external rain band.

References

1. Debi Iacovelli, cited 2018: The Saffir/Simpson Hurricane Scale: An Interview with Dr. Robert Simpson. [Available online at <https://novalynx.com/store/pc/Simpson-Interview-d53.htm>.]
2. Blake, S. E., Zelinsky, A. David., 2018: National hurricane center tropical cyclone report hurricane harveyAL092017, 77 pp.
3. Ulbrich, C. W., and L. G. Lee, 2002: Rainfall characteristics associated with the remnants of Tropical Storm Helene in upstate South Carolina. *Weather and Forecasting*, 17, 1257-1267.
4. Wang, M. J., K. Zhao, M. Xue, G. F. Zhang, S. Liu, L. Wen, and G. Chen, 2016: Precipitation microphysics characteristics of a Typhoon Matmo (2014) rainband after landfall over eastern China based on polarimetric radar observations. *J Geophys Res-Atmos*, 121, 12415-12433.
5. Didlake, A. C., and M. R. Kumjian, 2017: Examining Polarimetric Radar Observations of Bulk Microphysical Structures and Their Relation to Vortex Kinematics in Hurricane Arthur (2014). *Monthly Weather Review*, 145, 4521-4541.
6. May, P. T., J. D. Kepert, and T. D. Keenan, 2008: Polarimetric radar observations of the persistently asymmetric structure of Tropical Cyclone Ingrid. *Monthly Weather Review*, 136, 616-630.
7. Yu, C. K., and C. L. Tsai, 2013: Structural and Surface Features of Arc-Shaped Radar Echoes along an Outer Tropical Cyclone Rainband. *J Atmos Sci*, 70, 56-72.
8. Kumjian, M. R., and A. V. Ryzhkov, 2012: The Impact of Size Sorting on the Polarimetric Radar Variables. *J Atmos Sci*, 69, 2042-2060.
9. Ryzhkov, A., and Zrnicek, D., 2019: *Radar Polarimetry for Weather Observations*. Springer International Publishing, 486 pp.
10. Tourville, N., G. Stephens, M. DeMaria, and D. Vane, 2015: Remote Sensing of Tropical Cyclones: Observations from CloudSat and A-Train Profilers. *B Am Meteorol Soc*, 96, 609-622.
11. Wu, S. N., and B. J. Soden, 2017: Signatures of Tropical Cyclone Intensification in Satellite Measurements of Ice and Liquid Water Content. *Monthly Weather Review*, 145, 4081-4091.
12. Goren, T., and D. Rosenfeld, 2012: Satellite observations of ship emission induced transitions from broken to closed cell marine stratocumulus over large areas. *J Geophys Res-Atmos*, 117.
13. Lensky, I. M., and D. Rosenfeld, 2008: Clouds-Aerosols-Precipitation Satellite Analysis Tool (CAPSAT). *Atmos Chem Phys*, 8, 6739-6753.
14. Rosenfeld, D., 2018: Chapter 6 - Cloud-Aerosol-Precipitation Interactions Based of Satellite Retrieved Vertical Profiles of Cloud Microstructure. *Remote Sensing of Aerosols, Clouds, and Precipitation*, T. Islam, Y. Hu, A. Kokhanovsky, and J. Wang, Eds., Elsevier, 129-152.
15. Rosenfeld, D., and I. M. Lensky, 1998: Satellite-based insights into precipitation formation processes in continental and maritime convective clouds. *B Am Meteorol Soc*, 79, 2457-2476.
16. Zhu, Y. N., D. Rosenfeld, X. Yu, G. H. Liu, J. Dai, and X. H. Xu, 2014: Satellite retrieval of convective cloud base temperature based on the NPP/VIIRS Imager. *Geophys Res Lett*, 41, 1308-1313.
17. Chang, W.-Y., W.-C. Lee, and Y.-C. Liou, 2015: The Kinematic and Microphysical Characteristics and Associated Precipitation Efficiency of Subtropical Convection during SoWMEX/TiMREX. *Monthly Weather Review*, 143, 317-340.
18. Gadelmawla, E. S., M. M. Koura, T. M. A. Maksoud, I. M. Elewa, and H. H. Soliman, 2002: Roughness parameters. *J Mater Process Tech*, 123, 133-145.

19. Bukovcic, P., A. Ryzhkov, D. Zrnica, and G. F. Zhang, 2018: Polarimetric Radar Relations for Quantification of Snow Based on Disdrometer Data. *J Appl Meteorol Clim*, 57, 103-120.
20. Griffin, E. M., T. J. Schuur, and A. V. Ryzhkov, 2018: A Polarimetric Analysis of Ice Microphysical Processes in Snow, Using Quasi-Vertical Profiles. *J Appl Meteorol Clim*, 57, 31-50.
21. Kumjian, M. R., and K. A. Lombardo, 2017: Insights into the Evolving Microphysical and Kinematic Structure of Northeastern US Winter Storms from Dual-Polarization Doppler Radar. *Monthly Weather Review*, 145, 1033-1061.
22. Ryzhkov, A., P. F. Zhang, H. Reeves, M. Kumjian, T. Tschallener, S. Tromel, and C. Simmer, 2016: Quasi-Vertical Profiles-A New Way to Look at Polarimetric Radar Data. *J Atmos Ocean Tech*, 33, 551-562.
23. Tobin, D. M., and M. R. Kumjian, 2017: Polarimetric Radar and Surface-Based Precipitation-Type Observations of Ice Pellet to Freezing Rain Transitions. *Weather and Forecasting*, 32, 2065-2082.
24. Fan J. and Coauthors, 2018: Substantial convection and precipitation enhancements by ultrafine aerosol particles. *Science*, 359, 411 - 418.
25. NOAA, cited 2018: How many direct hits by hurricanes of various categories have affected each state? [Available online at <http://www.aoml.noaa.gov/hrd/tcfaq/E19.html>.]
26. Wu, D., and Coauthors, 2018: Kinematics and Microphysics of Convection in the Outer Rainband of Typhoon Nida (2016) Revealed by Polarimetric Radar. *Monthly Weather Review*, 146, 2147-2159.